

Dissertation:

Applications of the multi-parametrical function of
photon registration efficiency in neutronics and
radiation monitoring

Slawomir Jednorog D.Sc., Eng.

The Gen. Sylwester Kaliski
Institute of Plasma Physics and Laser Microfusion

Warsaw 2017

CONTENTS:

1	A SERIES OF TWELVE MONOTHEMATIC PUBLICATIONS	4
2	INTRODUCTION	5
3	SELECTION OF MATERIAL AND METHODS	6
3.1	ENERGY-EFFICIENCY CALIBRATION OF DETECTOR	6
3.2	ANALYTICAL TOOLS ALLOWING THE ASSESSMENT OF THE EFFICIENCY FUNCTION .	6
4	MULTI-PARAMETRICAL EFFICIENCY FUNCTION	7
4.1	MOTION OF A POINT RADIATION SOURCE ALONG THE DETECTOR AXIS	7
4.2	CYLINDRICAL INDIUM SAMPLE DIAMETER EXPANSION.....	10
4.3	INCREASING THE HEIGHT OF THE CYLINDRICAL INDIUM SAMPLE.....	12
4.4	RADIATION SOURCES MADE FROM DIFFERENT METALS	13
4.5	REGISTRATION EFFICIENCY FOR PHOTONS EMITTED FROM FLAT CONTAMINATED SURFACES.....	15
4.6	DEPENDENCE OF REGISTRATION EFFICIENCY ON PHOTON DIRECTION.....	16
5	APPLICATION OF THE MULTI-PARAMETRIC FUNCTION OF REGISTRATION EFFICIENCY TO NEUTRONICS AND RADIATION MONITORING	17
5.1	EXAMINING THE DENSE DEUTERIUM MAGNETIZED PLASMA IN A PF-1000 PLASMA GENERATOR	17
5.1.1	<i>Neutron yield for PF-1000 plasma generator.....</i>	<i>17</i>
5.1.2	<i>Anisotropy of neutron emissions in the PF-1000 facility.....</i>	<i>18</i>
5.1.3	<i>Radial asymmetry in the neutron emission for the PF-1000 device</i>	<i>19</i>
5.2	MONITORING NEUTRON YIELD Y_N FOR THE 14-MeV NEUTRON GENERATOR.....	21
5.3	INVESTIGATING NEUTRON EMISSIONS FROM DEUTERIUM PLASMA PRODUCED IN THE JET TOKAMAK	22
5.4	ENVIRONMENTAL RADIATION MONITORING	23
6	ACCURACY	24
7	CONCLUSIONS.....	24

1 A series of twelve monothematic publications

- M 1 **Jednorog S**, Szydłowski A, Scholz M, Paduch M, Bienkowska B (2012) Preliminary determination of angular distribution of neutrons emitted from PF-1000 facility by indium activation, [Nukleonika \(2012\) 57\(4\) 563-568](#)
http://www.nukleonika.pl/www/back/full/vol57_2012/v57n4p563f.pdf
- M 2 **Jednorog S**, Szydłowski A, Bienkowska B, Prokopowicz R (2014), The application of selected radionuclides for monitoring of the D–D reactions produced by dense plasma-focus device, [J Radioanal Nucl Chem, \(2014\) 301:23–31](#)
DOI 10.1007/s10967-014-3131-0
- M 3 Ciupek K, **Jednorog S**, Fujak M, Szewczak K (2014) Evaluation of efficiency for in situ gamma spectrometer based upon cerium-doped lanthanum bromide detector dedicated for environmental radiation monitoring, [J Radioanal Nucl Chem \(2014\) 299:1345–1350](#)
DOI 10.1007/s10967-013-2906-z
- M 4 **Jednorog S**, Paduch M, Szewczak K, Laszyska E (2015) Radioindium and determination of neutron radial asymmetry for the PF-1000 plasma focus device, [J Radioanal Nucl Chem \(2015\) 303:941–947](#)
DOI 10.1007/s10967-014-3444-z
- M 5 **Jednorog S**, Ciupek K, Krajewski P, Łaszyńska E, Ziółkowski A (2015) Calibration of the angular energy efficiency of an in situ spectrometer based on a LaBr3(Ce) detector, [J Radioanal Nucl Chem \(2015\) 303, 3-5.](#)
DOI 10.1007/s10967-014-3444-z
- M 6 Laszyska E, **Jednorog S**, Ziolkowski A, Gierlik M, Rzadkiewicz J (2015) Determination of the emission rate for the 14 MeV neutron generator with the use of radio-yttrium, [Nukleonika \(2015\) 60\(2\)](#)
DOI: 10.1515/nuka-2015-0040
- M 7 Prokopowicz R, Bienkowska B, Drozdowicz K, **Jednorog S**, Kowalska-Strzeciwiłk E, Murari A, Popovichev S, Pytel K, Scholz M, Szydłowski A, Syme B, Tracz G (2011) Measurements of neutrons at JET by means of the activation methods, [Nucl Instrum Meth A 637 \(2011\) 119–127](#)
DOI:10.1016/j.nima.2011.01.128
- M 8 **Jednorog S**, Laszyska E, Bienkowska B, Ziolkowski A, Paduch M, Szewczak K, Mikszuta K, Malinowski K, Bajdel M, Potrykus P (2017) A new concept of fusion neutron monitoring for PF-1000 device, [Nukleonika, 2017 62\(1\)](#)
DOI 10.1515/nuka-2017-0000
- M 9 **Jednoróg S** (2016) O zastosowaniu spektrometrii gamma w fizyce plazmy. Wczoraj i dziś promieniowania. (cz.2)
[Przegląd Techniczny-Gazeta Inżynierska, 19-20 \(2016\) 19-22](#)
- M 10 **Jednoróg S** (2016) Zastosowanie spektrometrii gamma w fizyce plazmy. Wieloparametryczne funkcje rejestracji fotonów - aspekt teoretyczny (cz.1),
[Przegląd Techniczny-Gazeta Inżynierska 22-23 \(2016\) 26-28](#)
- M 11 **Jednoróg S** (2016) Zastosowanie spektrometrii gamma w fizyce plazmy. Wieloparametryczne funkcje rejestracji fotonów - aspekt teoretyczny (cz.2),
[Przegląd Techniczny-Gazeta Inżynierska 25-26 \(2016\) 19-21](#)
- M 12 **Jednoróg S** (2017) Zastosowanie spektrometrii gamma w fizyce plazmy. Wieloparametryczne funkcje rejestracji fotonów - zastosowania praktyczne,
[Przegląd Techniczny-Gazeta Inżynierska 2-3 \(2017\) 29-31](#)

2 Introduction

The energy-efficiency calibration of a gamma spectrometer involves the determination of the photon registration efficiency function using experimental methods or numerical simulations. Before the numerical characterization (NCh) of a detector was accessible, the only way to make an energy-efficiency calibration was to use calibration sources. For the sources in use to date, however, their amounts are limited to strictly defined geometries and densities.

The complete description of a radiation source is composed of its shape, construction, atomic composition, and homogeneity, which I term its *source geometry*, and its position relative to the detector, termed the *measurement geometry*. The measured geometry also takes into account radiation absorbers if they are present between the source and detector.

The energy-efficiency calibration designed for a particular detector, source geometry, and measurement geometry is no longer valid even if just one of these factors is changed. The NCh of the particular detector is a detailed description, which considers all structural elements, their size, and their relative positioning. It provides the geometrical input for the numerical simulations [M1 - M12, J36, J37] that determine the photon registration efficiency. The precise NCh for a particular detector is usually prepared by the manufacturer at a cost comparable to the price of the detector. Typically, this is done for high-purity germanium (HPGe) detectors, although NCh(s) for scintillation detectors of NaI(Tl) and LaBr₃(Ce) are also available. I use two types of NCh: *dedicated* for a particular detector and *generic* for an array of detectors of the same type. The first gives very precise energy-efficiency calibrations (see Fig. 1) [M1, M10]; the second provides correct results but with a much larger uncertainty (see Fig. 2) [M5].

A mathematical energy-efficiency calibration gives researchers unlimited possibilities. The efficiency function can be determined in practice with high precision for any source shape and composition [M10, M11, R12]; it only requires the effective employment of a geometry composer, that is, the part of the software dedicated to the evaluation of efficiency. Good examples are the software packages *In Situ* Object Counting Systems (ISOCS) and Laboratory Sourceless Object Calibration Software (LabSOCS).

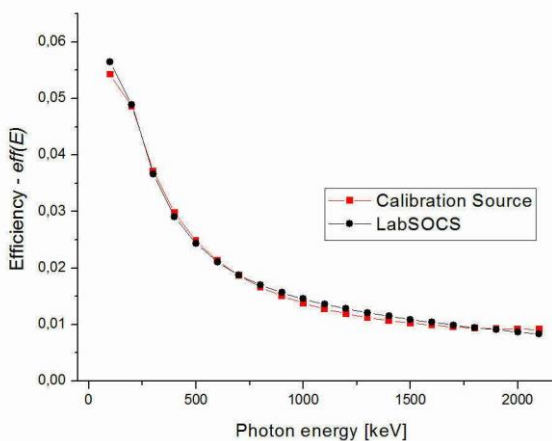


Fig. 1 Efficiency for the HPGe detector obtained by two methods using a dedicated NCh [M1, M10]

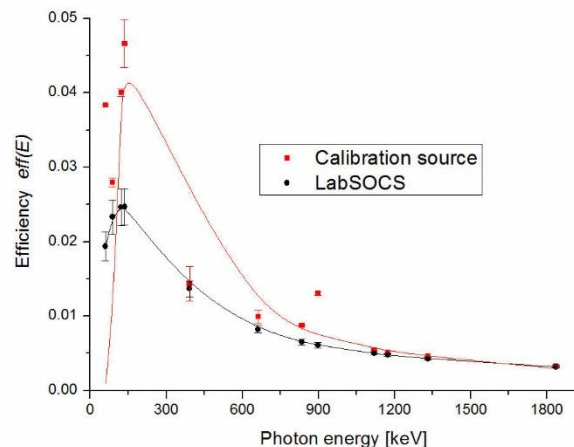


Fig. 2 Efficiency for LaBr₃(Ce) detector obtained by two methods using a generic NCh [M5]

The widespread use of a numerical simulation gives the owner of the detector a chance to compose its NCh, although it is possible to investigate later the detector efficiency given the sample geometry as well as measurement geometry. Nevertheless, the logical sequence of events should be useful to in the research process. The parameters that are very useful for neutronics are: the source distance to the endcap [M11], sample diameter, height, and the

source's material composition. The size of the contaminated area [M3] and the direction of incident photons [M5] are parameters that are important for radiation monitoring. The assessment of the multi-parametric detector efficiency function provides information that allows the successful investigation of many scientific tasks.

3 Selection of material and methods

3.1 Energy-efficiency calibration of detector

The quantity that describes the number of detected photons is the absolute full energy peak (AFEP)—the net area (total area minus background count area) of the full energy absorption peak. The detector efficiency for γ detection is defined as the ratio of the number of photons effectively registered by a detector to that emitted by a radiation source. Because the detector efficiency strongly depends on energy, it should be expressed as a function of photon energy $eff(E)$. This function is strongly nonlinear.

The objective of γ -spectrometry is to measure the AFEPs and assess the activity of a particular radionuclide that comprises the sample of a certain geometry. For this purpose, the AFEP efficiency (AFEPE) must also be known. Hence, the term efficiency hereafter refers to AFEPE, unless otherwise stated in which event the definition of the particular expression is evoked. The AFEPE is expressed as the ratio of the count rate to the product of the activity of the calibration source and the probability that a photon of a particular energy is released by the nucleus.

3.2 Analytical tools allowing the assessment of the efficiency function

Without empirical support, it is hard to predict how a particular radiation sample should be measured to obtain a higher count rate, i.e., $AFEP \cdot s^{-1}$. Nevertheless, the best approach is to assume that the measurement geometry leads to higher count rate. When the radiation source emits only mono-energetic photons, it suffices to compare AFEPs obtained in the results of a source survey with different measurement geometries but taken at this same measurement time. Nonetheless, photons of different energies are usually released by a radiation source. If the branching ratios of such photons are comparable, it is not easy to say which photon energy is the reference. A similar situation takes place when the source is composed of many radionuclides. In that case the better-measured geometry is that which results in the larger area below the efficiency curve. Hence the Riemann integral of the efficiency function $eff(E)$ over an energy interval dE with the limit of integration corresponding to the detector sensitivity enables two different measurement geometries to be compared. The above dimensionless quantity is expressed by equation). I am the first to introduce the term “integrated absolute full energy peak efficiency” (IAFEPE) [M3].

$$IAFEPE = \int_{E_{\min}}^{E_{\max}} eff(E) dE \quad (1)$$

$$MIAFEPE = m \cdot \int_{E_{\min}}^{E_{\max}} eff(E) dE \quad (2)$$

$$SIAFEPE = s \cdot \int_{E_{\min}}^{E_{\max}} \text{eff}(E) dE \quad (3)$$

One of many tasks in neutronics is to register neutrons. A specific example of indirect neutron registration is in the survey of the activity level induced in an irradiated sample by neutrons. That measurement allows an assessment of the neutron yield Y_n of a device and through deconvolution, the neutron energy spectrum [M2, M6, M7].

The "mass-integrated absolute full energy peak efficiency" (MIAFEPE) (see equation (2)) is a parameter that combines the possibility of activation of a sample and its effectively measurement using γ -spectrometry. The MIAFEPE is the product of sample mass and IAFEPE [M12].

"Superficial integrated absolute full energy peak efficiency" (SIAFEPE) is the product of the IAFEPE and the area of the contaminated surface (see equation (3)), which is a quantity that is useful for environmental radiation monitoring [M3].

4 Multi-parametrical efficiency function

4.1 Motion of a point radiation source along the detector axis

I have analyzed the virtual motion of a point radiation source along the detector axis (see Fig. 3) [M10]. Here the initial position occupied by the source is assumed to be on the detector endcap and the final position is located at a distance sufficiently far away. At each successive position of the radiation source the efficiency in photon registration is slightly smaller than before.

The efficiency is well-known to be better when the source is closer to the detector. Nevertheless, IAFEPE is a useful quantity allowing the tracking of changes in efficiency. This frees up the need to track changes in the measurement geometry that lead to a better or worse registration efficiency of the γ radiation.

Although the motion of the source is quantified, the value of the particular quantity is described by Δl_i . The subscript i is added to emphasis that any two motions are not identical. Contrary to the previous declaration, the radiation source does not reach infinity. It stops at some position from where the radiation is still able to reach the detector and possible detection. I assess the efficiency specific for each source location. This implies that for all source locations I perform a mathematical energy-efficiency calibration of the detector. The calculations were performed using the program LabSOCS and the detector NCh.

For a particular detector and point-like radiation source held at fixed locations l_i , the values of the efficiencies for different photon energies E_i are calculated and stored in an array, $\text{eff}(l_i, E_j)$. This array is displayed in equation (4) [M10]. The meaning of the quantities appearing are as follows: l_i - source endcap distance ($i = 1, 2, \dots, n$); E_j - the photon energies that are of interest in the efficiency calculation ($j = 1, 2, \dots, m$).

In this way, the detector efficiency that is usually dependent on the photon energy E depends now on the distance between point radiation source and endcap l . By combining subsequent efficiency graphs into one drawing, a three-dimensional (3D) map is obtained. This map presents the dependence of the photon registration efficiency on photon energy and point radiation source and endcap distance (Fig. 9) [M12, R12].

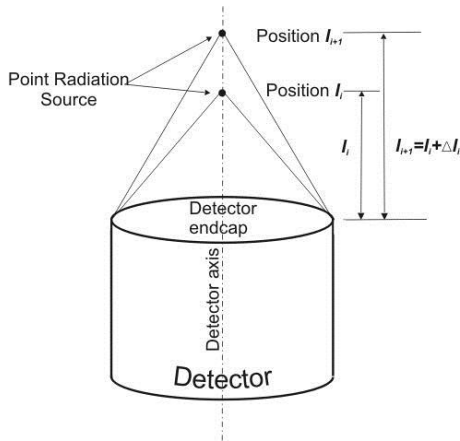


Fig. 3 Motion of a point radiation source along the detector axis. [M10]

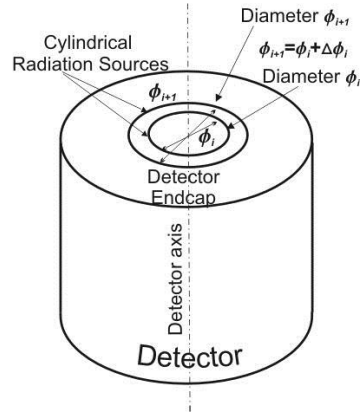


Fig. 4 Changes in the diameter for a cylindrical radiation source made from indium. [M11]

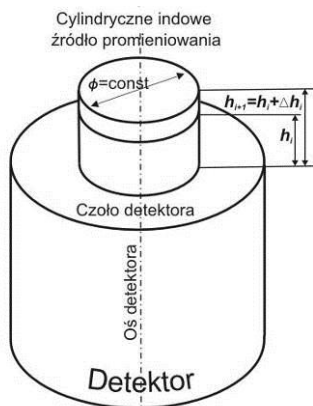


Fig. 5 Changes in the height for a cylindrical radiation source made from indium [M11]

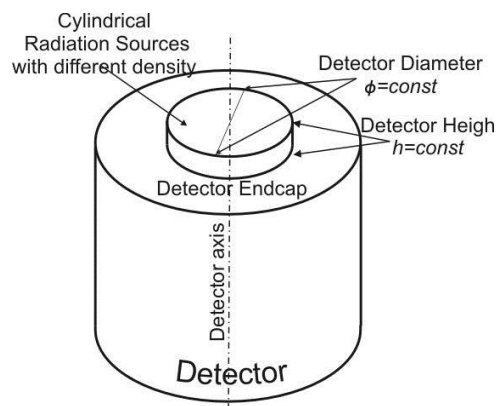


Fig. 6. Activation sample with different atomic composition (density) [M11]

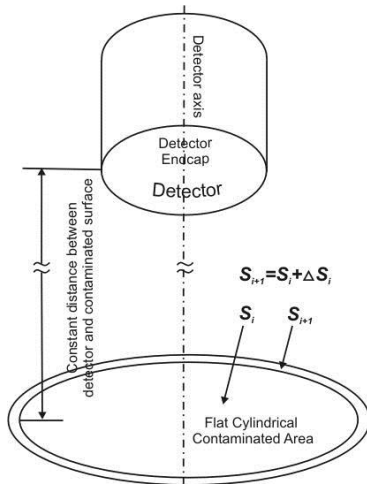


Fig. 7 Flat circular surface with changing size (diameter)

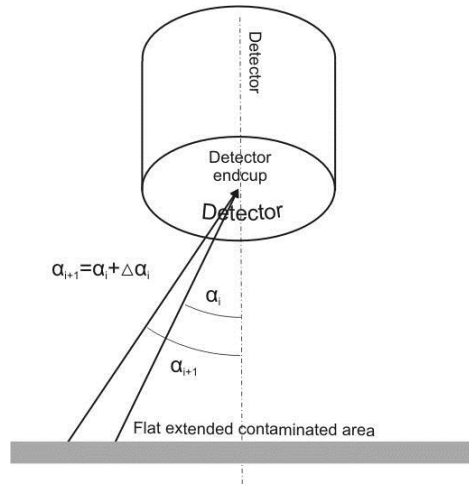


Fig. 8 Angular changes related to radiation reaching the detector

The function $eff(l, E)$ determines the two-parameter efficiency function whereas $eff(l_i, E_j)$ is its value for a radiation source at a distant l_i from the detector endcap emitting a photon of energy E_j . Either of these two quantities can be held constant or varied. Also, it is not important whether we have an analytical expression of the function $eff(l, E)$.

$$eff(l_i, E_j) = \begin{cases} eff(l_1, E_1) & eff(l_1, E_2) & \dots & eff(l_1, E_m) \\ eff(l_2, E_1) & eff(l_2, E_2) & \dots & eff(l_2, E_m) \\ \vdots & \vdots & \vdots & \vdots \\ eff(l_n, E_1) & eff(l_n, E_2) & \dots & eff(l_n, E_m) \end{cases}$$

(4)

$$eff(\phi_i, E_j) = \begin{cases} eff(\phi_1, E_1) & eff(\phi_1, E_2) & \dots & eff(\phi_1, E_m) \\ eff(\phi_2, E_1) & eff(\phi_2, E_2) & \dots & eff(\phi_2, E_m) \\ \vdots & \vdots & \vdots & \vdots \\ eff(\phi_n, E_1) & eff(\phi_n, E_2) & \dots & eff(\phi_n, E_m) \end{cases}$$

(5)

$$eff(h_i, E_j) = \begin{cases} eff(h_1, E_1) & eff(h_1, E_2) & \dots & eff(h_1, E_m) \\ eff(h_2, E_1) & eff(h_2, E_2) & \dots & eff(h_2, E_m) \\ \vdots & \vdots & \vdots & \vdots \\ eff(h_n, E_1) & eff(h_n, E_2) & \dots & eff(h_n, E_m) \end{cases}$$

(6)

$$eff(\rho_i, E_j) = \begin{cases} eff(\rho_1, E_1) & eff(\rho_1, E_2) & \dots & eff(\rho_1, E_m) \\ eff(\rho_2, E_1) & eff(\rho_2, E_2) & \dots & eff(\rho_2, E_m) \\ \vdots & \vdots & \vdots & \vdots \\ eff(\rho_n, E_1) & eff(\rho_n, E_2) & \dots & eff(\rho_n, E_m) \end{cases}$$

(7)

$$eff(S_i, E_j) = \begin{cases} eff(S_1, E_1) & eff(S_1, E_2) & \dots & eff(S_1, E_m) \\ eff(S_2, E_1) & eff(S_2, E_2) & \dots & eff(S_2, E_m) \\ \vdots & \vdots & \vdots & \vdots \\ eff(S_n, E_1) & eff(S_n, E_2) & \dots & eff(S_n, E_m) \end{cases}$$

(8)

$$eff(\alpha_i, E_j) = \begin{cases} eff(\alpha_1, E_1) & eff(\alpha_1, E_2) & \dots & eff(\alpha_1, E_m) \\ eff(\alpha_2, E_1) & eff(\alpha_2, E_2) & \dots & eff(\alpha_2, E_m) \\ \vdots & \vdots & \vdots & \vdots \\ eff(\alpha_n, E_1) & eff(\alpha_n, E_2) & \dots & eff(\alpha_n, E_m) \end{cases}$$

(9)

The highest value of the AFEPE is recorded when the radiation source is placed on the detector endcap [M9]. On increasing the sample–endcap distance, the solid angle within which radiation reaches the detector decreases. This leads to a decrease in the ratio between detector surface area and the surface of the sphere into which radiation is emitted and subsequently influences the geometrical efficiency factor [M5].

If, after neutron irradiation, the radioactivity of sample is high enough, the sample must be appropriately surveyed because of the short half-life of the obtained radionuclide as the only way to reduce the dead-time is to move the sample away from the endcap. This is the simplest example of an application of the multi-parametric function for the photon registration efficiency where it depends on photon energy and source–detector distance.

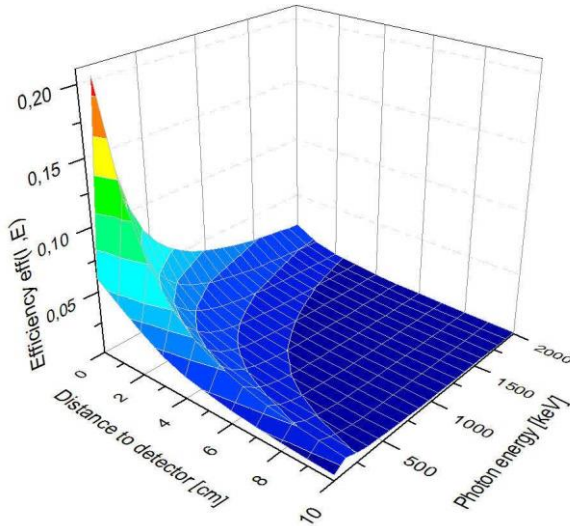


Fig. 9 Efficiency as a function of photon energy and distance between a point radiation source and a HPGe detector [M12]

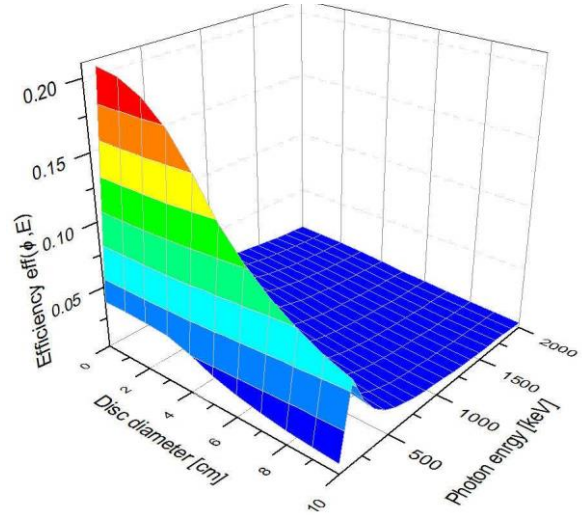


Fig. 10 Efficiency as a function of photon energy and diameter between a cylindrical indium sample and HPGe detector [M12]

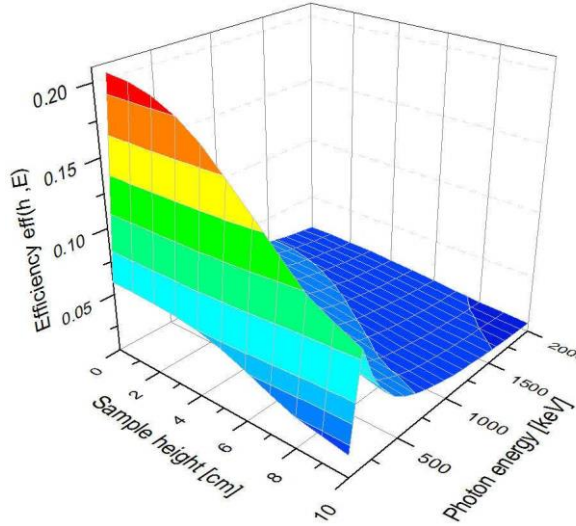


Fig. 11 Efficiency for the HPGe detector as a function of photon energy and height of a cylindrical indium source [M12]

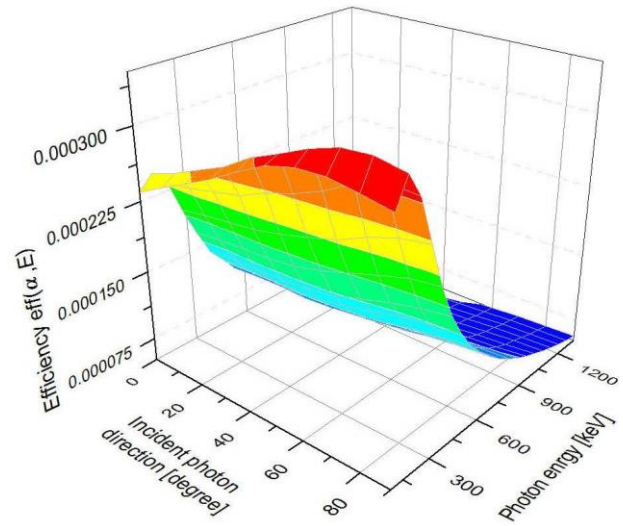


Fig. 12 Influence of the photon energy and direction on efficiency for a LaBr₃(Ce) detector [M3]

4.2 Cylindrical indium sample diameter expansion

Indium is frequently used as a 2.45-MeV neutron monitor in investigations of deuterium plasmas. The nuclear reaction $^{115}\text{In}(n,n')^{115m}\text{In}$ has a significant importance as a means to monitor the total neutron yield Y_n at the Joint European Torus (JET) machine [M7, R12] as well as other devices running deuterium plasma experiments [M2]. In a mixture of stable indium isotopes, 95.7% is ^{115}In . The inelastic scattering reaction $^{115}\text{In}(n,n')^{115m}\text{In}$ has i) a suitably located threshold $E_n=339$ keV that allows the registration of neutrons obtained from the reaction (d,d), ii) a sufficiently high cross section, and iii) a product with a sufficiently long half-life ($T_{1/2}=4.486$ h) [M2].

Based on the above, I took into consideration the cylindrical geometry of the indium radiation source. During virtual experiments the source was placed on the endcap of a HPGe detector supplied with a NCh. The cylinder was assumed to be a thin disc infinitesimal in height with a varying diameter (see Fig. 4) [M11]. In the initial stage, this disc had both infinitesimal height and diameter but in the final stage it becomes very thin but with infinitely large diameter. I verified that the limit procedure for the diameter was valid. Indeed, the expanding diameter in this limit does not lead to an increase in efficiency.

The array described by equation (5) [M11] consists of elements $eff(\phi_i, E_j)$, each of which determines the detection efficiency for a photon of energy E_j that has left the sample at diameter ϕ_i and afterwards is registered by the detector HPGe of known NCh. The row of the array thus consists of assessments of the efficiency as a function of increasing energy. When the photons leave the indium radiation source at diameter $\phi_i = const$, the source nevertheless is still very thin. The following row of the array consists of efficiency values for the subsequent disc, but this time with diameter $\phi_{i+1} = \phi_i + \Delta\phi_i$. The quantity $\Delta\phi_i$ corresponds to the slight increase in diameter between successive changes. Introducing the subscript i to $\Delta\phi_i$ emphasizes the point that further differences are not equal. Moving down the columns of the array, one observes the dependence of efficiency on changes in the diameter of the disk for fixed photon energy $eff(\phi_i, E_j = const)$.

The subsequent 3D map (see Fig. 10) shows the dependence of the photon registration efficiency on the indium disc diameter and photon energy. Each graph resulting from the above procedure represents the dependence of registration efficiency for a series of samples with

various diameters and constant photon energy $eff(\phi, E_j=const)$. The numerical data for the above graphs are easy accessed because they are present in sequenced columns of the array in equation (5). Fig. 14 sketches the analysis of the efficiency for a fixed photon energy $E=45$ keV. The set of points has been successfully interpolated as a Gaussian function (equation (10)),

$$D(\phi, E = const) = y_0 + \sqrt{\frac{\pi}{2}} \cdot \frac{A \cdot \exp\left(-\frac{2(\phi - \phi_c)^2}{w^2}\right)}{w}, \quad (10)$$

where: ϕ is the disc diameter of the indium sample, ϕ_c , y_0 , and w are fitting parameters [R12].

Analysis of the second derivative of this function enables the inflection point to be determined and the convex and concave part of the curve to be identified (see Fig. 14) [M12, R12]. The inflection point has an associated physical meaning in that it defines precisely the diameter of activation sample ϕ_i . The efficiency in registering the photon (released from ^{115m}In nuclei) for the measurement geometry covering this exact sample has a higher value. That is, photons emitted from samples of larger or smaller diameter are registered by a particular detector with poorer efficiency! The location of the inflection point depends on the photon energy but over a limited range (see Fig. 15) [M12, R12]. Photons with energies 336 keV and 391 keV were emitted from an indium activation sample and were released from the nuclei of ^{115m}In and ^{113m}In . The most important are photons released during de-excitation of the ^{115m}In nuclei.

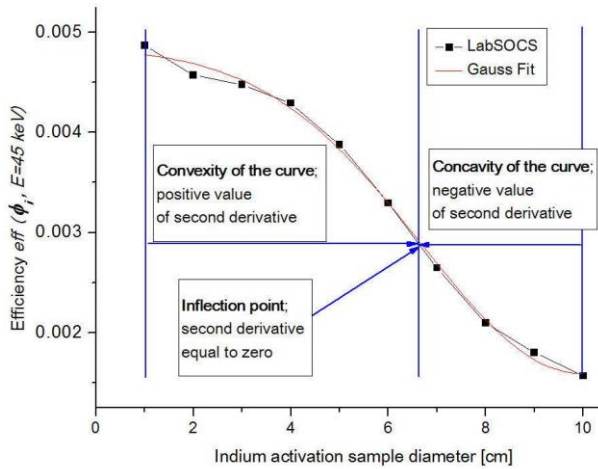


Fig. 14 Mathematical analysis of the function describing the diameter dependence of the detector efficiency for registration of a photon emitted from an indium sample provides important information [M12, R12]

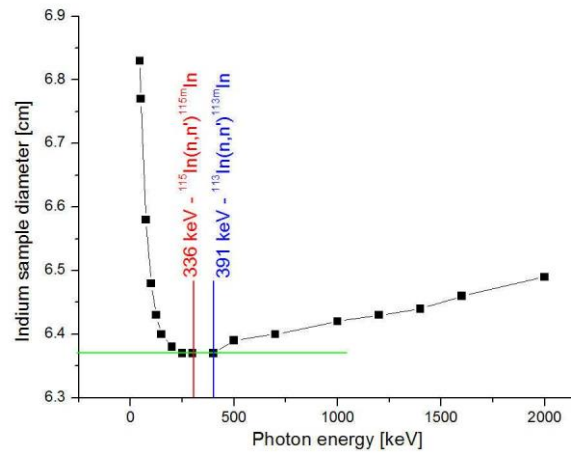


Fig. 15 Values of the second derivative of the efficiency function (having a dependence on disc diameter) describing the set of maximal values of efficiency for various indium sample diameters at fixed photon energy. [M1, R12]

For the purpose of determining the value of the optimal sample diameter, some measures were taken into account. The inflection point that results by identifying the minimum (on the red line) and perpendicularly projecting (green line) back to the ordinate. The red line marks a photon energy $E_\gamma = 336$ keV. As a result, I determined that for this particular detector the value

of optimal diameter for indium activation sample is $\phi = 63.7$ mm. Thereafter, this sample was used many times [M1, M2, M4].

The presented case is quite simple. The energies of photons emitted from nuclei formed during neutron activation of an indium target ^{115m}In , as well as ^{113m}In , lie close to each other. Apart from the above-mentioned isotopes of indium, the others that are the result of radiative capture appear too. Their usefulness for neutronics though is limited by comparison. If the radionuclide formed during activation emits photons with energies significantly different, this should be considered separately.

4.3 Increasing the height of the cylindrical indium sample

I analyzed a virtual cylindrical radiation source made from indium. With the source diameter constant $\phi_{j=const}$, I located this source on the detector endcap and then varied the source height (Fig. 5). I assumed that in the initial stage of the experiment the disc had an infinitesimal height subject to variation Δh_i ; the subsequent height is then $h_{i+1} = h_i + \Delta h_i$ which describes the incremental change in height.

Calculations relating to the HPGe detector with NCh were made using the software LabSOCS. The procedure required repetitions for each height to fill the array $eff(h_i, E_j)$ represented by equation (6) [M11].

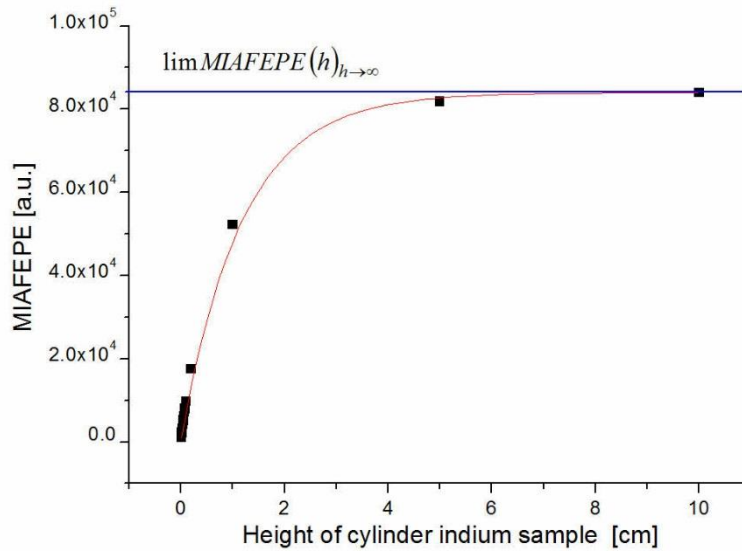


Fig. 16 Unlimited increase in height of the radioactive source made of indium does not lead to an increase in registration efficiency. MIAFEPE has an asymptotic limit

Using the procedure outlined above, I plotted a 3D map representing the dependence of the efficiency $eff(h, E)$ on the energy E of the emitted photons and the height h of the cylindrical sample (Fig. 11). The investigative procedures are enriched by introducing an analysis of MIAFEPE. The objective is to analyze the row of the array $eff(h_{i=const}, E_j)$. The values presented there were interpolated with a polynomial in the logarithmic function giving the best fit. The obtained function was integrated over the interval corresponding to the energy sensitivity of the detector. The MIAFEPEs for successive samples were then determined using equation (2). It turns out that a sequence of MIAFEPEs can be interpolated using an increasing exponential function and has a limit (Fig. 16) [M12]. Importantly, its physical meaning is that the activation sample is restrained in height and its increase is not accompanied by an increase in registration efficiency.

4.4 Radiation sources made from different metals

Next, a cylindrical metallic radiation source of fixed diameter $\phi=18$ mm and height $h=1$ mm (standard JET) is considered. I chose different metals for the composition of samples. That resulted in a change in density ρ . This is important because even a small change in sample density leads to a significant change in efficiency (Fig. 17A) [M12, R12].

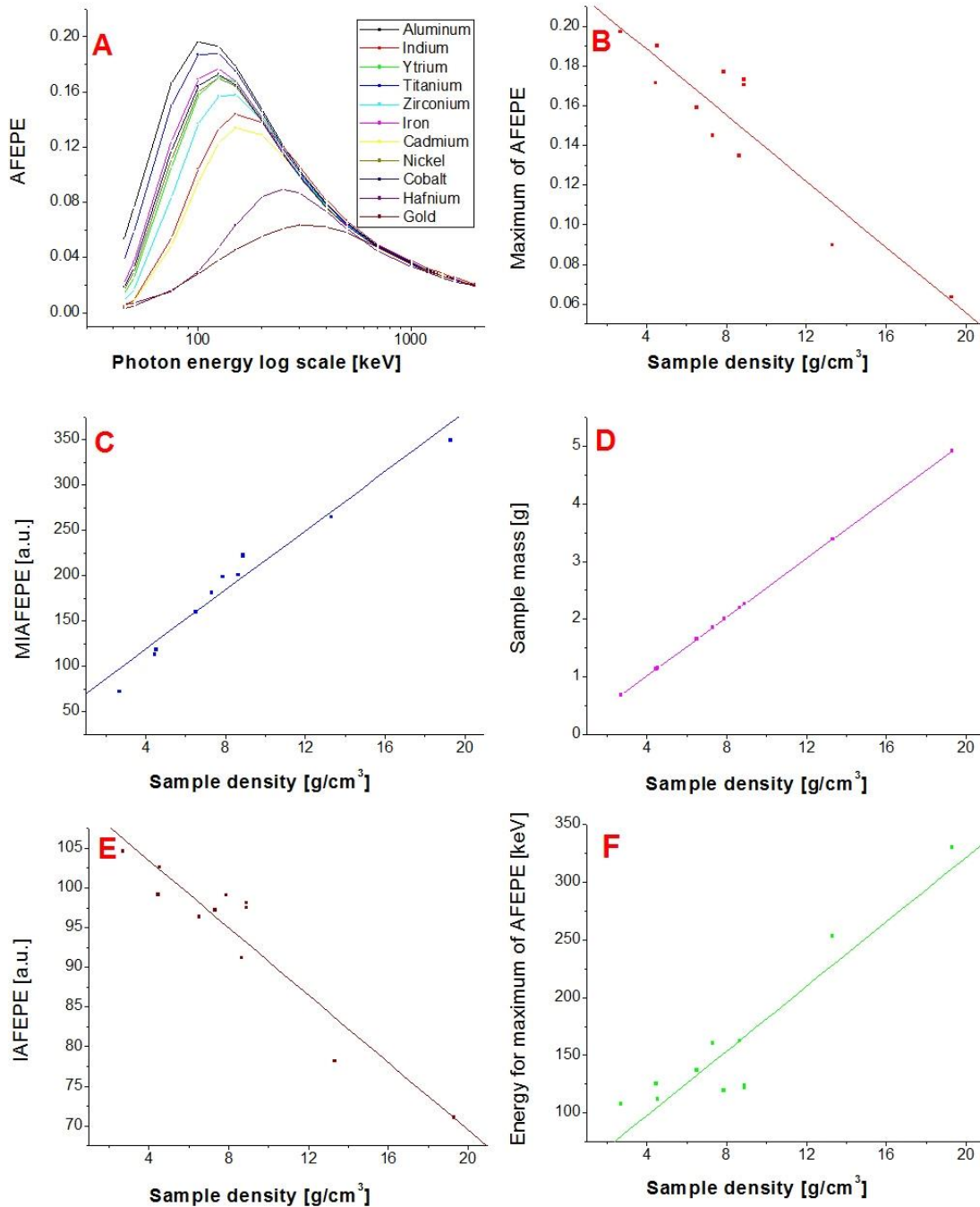


Fig. 17 Changing the material (metal), from which the activation sample was made, leads to significant changes in photon registration efficiency

Each step of the procedure was similar to the activities presented in Chapter 4.1–4.3. The final product of the procedure was an array of $eff(\rho_i, E_j)$ as in equation (7) [M11, R12] containing the dependence of the efficiency on the density of the sample and the emitted photon energy.

I calculated the values of AFEPE, IAFEPE, and MIAFEPE. The above and maximum values of AFEPE, the energies for the maximum values of AFEPE, and sample mass as a function of density are presented in Fig. 17A–F. For the samples having extreme density values (aluminum and gold), the AFEPE changed three times (Fig. 17A), whereas the MIAFEPE increased seven times (Fig. 17C) with a tenfold increase in sample weight (Fig. 17D). Simultaneously, an increase in the density of the sample decreases IAFEPE (Fig. 17E). A diminishing efficiency in photon registration with increasing sample weight was compensated by an increase in weight, which grew faster than the decreasing efficiency. With increasing sample density, the maximum efficiency shifted towards higher energies (Fig. 17B). The energies associated with the efficiency maxima also increased (Fig. 17F).

From the above considerations related to samples made of pure metals, the results indicate that samples prepared as mixtures of metals could affect the value of the registration efficiency of photons emitted from the sample [M12, R12]. Nevertheless, the preparation of the mixed samples depends on properties of the parent metals. It should result from knowing the reaction rate [M6], neutron emission rate, and neutron energy spectrum. One needs the nuclear properties of the generated radionuclides such as half-lives, the position of the AFEP relative to other peaks, and the Compton background.

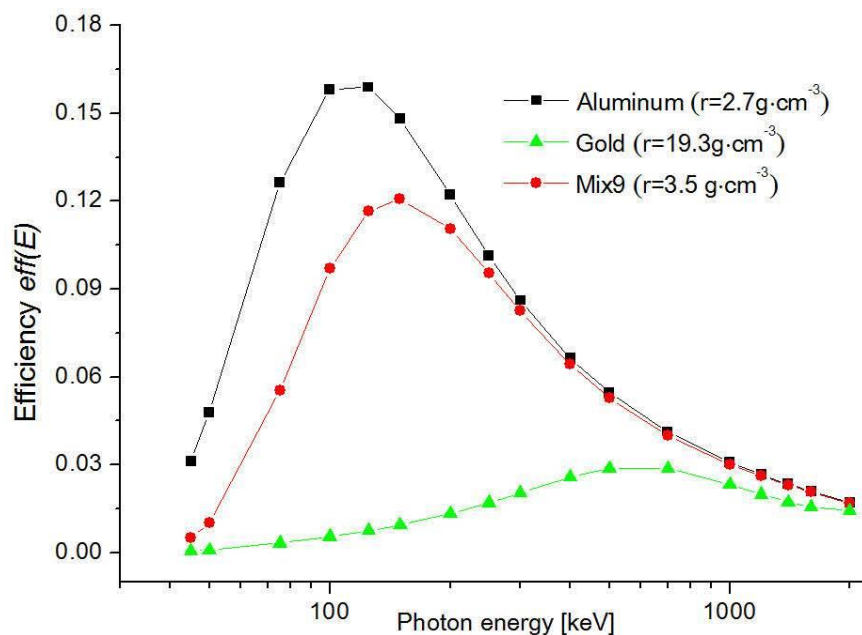


Fig. 18 Selecting the proportion of elements composing the activation sample, one can affect the photon registration efficiency. Sample Mix9 [Y (48%), Se (16%), Al (16%) Fe (20%)] was successfully used during experimental campaign at JET tokamak [M7, J36]

4.5 Registration efficiency for photons emitted from flat contaminated surfaces

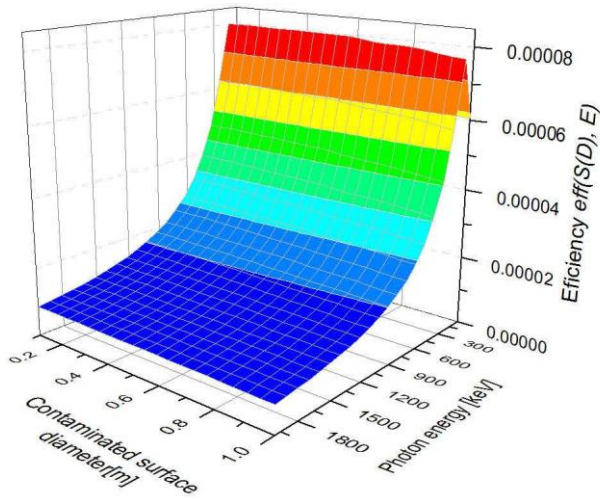


Fig. 19 Changes in registration efficiency for contaminated surfaces with various diameters in the range 0.1-1.0 m [M3]

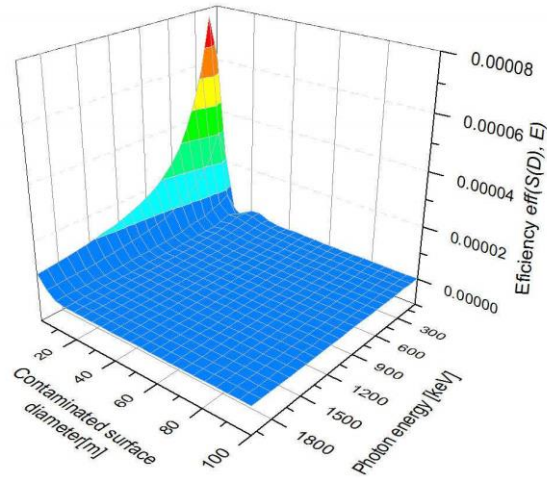


Fig. 20 Changes in registration efficiency for contaminated surfaces with various diameters in the range 1-100 m [M3]

Using the multi-parametric function for the photon registration efficiency, I completed an analysis that is useful in radiation monitoring of the environment. I considered the registration efficiency of photons emitted from a contaminated surface of increasing surface area (represented by the diameter of a circle). In numerical simulations, it is difficult to draw up a set of input data including infinite diameter. Therefore, in studying the behavior of the function describing the efficiency as the surface increases, I sought to know the behavior at infinity. This problem is illustrated in Fig. 7. The array described by equation (8) includes the values of registration efficiency $eff(S_i, E_j)$, which depend on the surface area of the contaminated region S_i and the photon energy E_j . To the successive rows of the array described by equation (8), I entered the values of the photon registration efficiency for subsequent circular areas that differ from each other by ΔS_i .

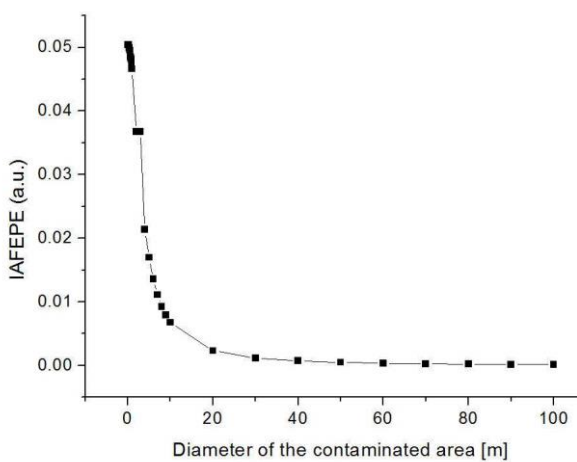


Fig. 21 IAFEPE analysis shows that that a threshold diameter exists for the contaminated surface area above which the detector efficiency does not change [M3]

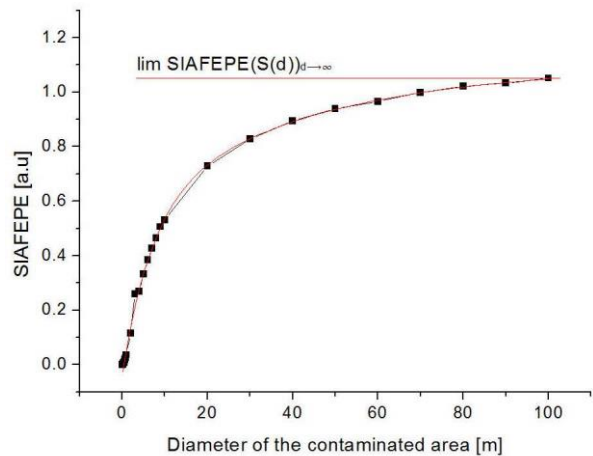


Fig. 22 Interpolation function describing the SIAFEPE has a limit. This implies that there is a certain size in contaminated area, outside of which radiation no longer reaches the detector [M3]

The procedure that describes the volatility of the area from which the radiation arrives at the detector has been presented earlier. Here, I focus on the photon registration efficiency of the detector equipped with a 1.5' scintillator $\text{LaBr}_3(\text{Ce})$ supplied with a generic NCh. The focus of the analysis is on the changes in efficiency as a function of the surface contaminated area. [Fig. 19](#) and [Fig. 20](#) show changes in the efficiency registration of photons emitted from contaminated surfaces with diameters varying between 0.1 m and 1 m, and from 1 to 100 m, respectively.

With consecutive rows of the array described by equation (8), I calculated both IAFEPE and SIAFEPE. The results are plotted in [Fig. 21](#) and [Fig. 22](#).

I have demonstrated in this way that there is a certain area outside of which the radiation is no longer recorded by the detector. This indicates that the interpolation function describing SIAFEPE has a limit, and hence it is possible to find the diameter of this area and the parameter values of the universal efficiency curve for this detector.

4.6 Dependence of registration efficiency on photon direction

Concerning the parameterization of the function of registration efficiency, I performed an analysis considering its dependence on the angle of incidence of the radiation ([Fig. 8](#)). The analysis focuses on the array of the registration efficiency that refers to the angle of incidence for the photons and their energy $eff(\alpha_i, E_j)$ as given in equation (9). The 3D map of these changes is presented in [Fig. 12](#).

In analyzing the variation in the geometric coefficient (see [Fig. 23](#)) [M5] on which the registration efficiency depends, I became aware that this function may have local extremes (see [Fig. 24](#)). This is important as it determines the position of the detector relative to the surface of the contaminated area. Efficiency values for fixed photon energy and varying direction of incidence for the radiation were interpolated, and then the function was examined and positions of the extremes were determined. The results presented in [Fig. 24](#) show that there are certain directions for which the photons reaching the detector are more efficiently recorded.

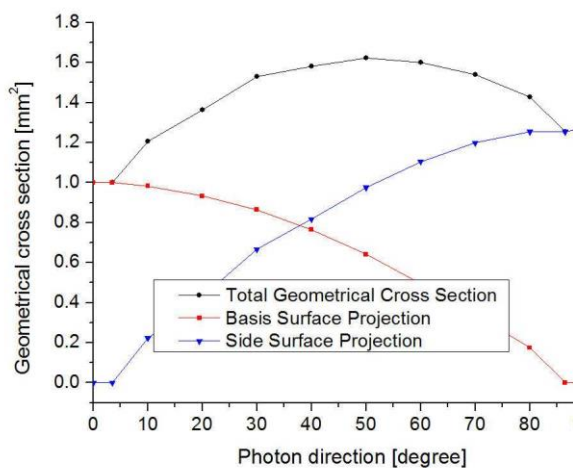


Fig. 23 Geometrical efficiency factor for the 1.5' $\text{LaBr}_3(\text{Ce})$ detector [M5]

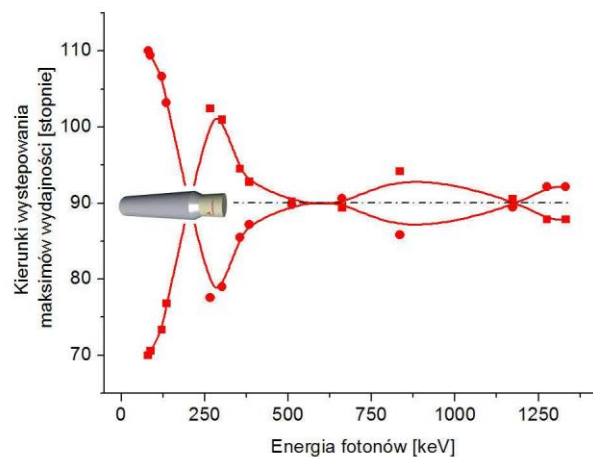


Fig. 24 For the efficiency function, there are local extremes that manifest themselves at particular photon directions and energies [M5]

5 Application of the multi-parametric function of registration efficiency to neutronics and radiation monitoring

5.1 Examining the dense deuterium magnetized plasma in a PF-1000 plasma generator

5.1.1 Neutron yield for PF-1000 plasma generator

I used a methodology for massive activation samples, to be described in Section 4.2, to manufacture an yttrium activation sample based on which was constructed the fast-neutron yttrium monitor (FNYM) serving as a monitor of the total neutron yield Y_n for the PF-1000 device. The FNYM measures Y_n during a single plasma discharge [M2, M8]. The following nuclear reaction: $^{89}\text{Y}(n,n')^{89m}\text{Y}$ is applied. Neutrons emitted from the PF-1000 device activate the yttrium sample, which has a mass of 114.74 grams. The sample is permanently attached to a 3' NaI(Tl) scintillation detector supplied with a generic NCh. The structure of the device is shown in Fig. 25; the FNYM fixed to the wall of PF-1000 is pictured in Fig. 26.

From Monte Carlo N-particle (MCNP) simulations, the activation coefficient for ^{89m}Y was calculated from data generated by modeling the activation of a “one-source” neutron during a single PF-1000 discharge. This value is estimated at $2.46 \cdot 10^{-29}$. Then Y_n is calculated by dividing by the amount of radioactivity caused in the yttrium sample through activation during a single discharge calculated using the MCNP code for one neutron source. I found a linear dependence for activation induced in yttrium as function of neutron yield, which was determined by the silver activation counters and the beryllium activation counter [M2].

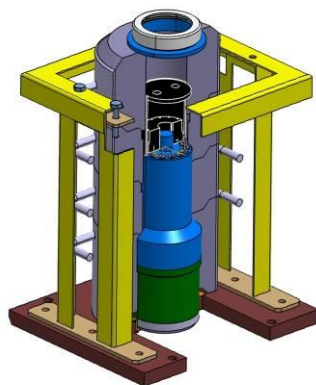


Fig. 25 Design of the FNYM: 3' scintillation detector NaI(Tl) (green), photomultiplier (blue), lead shielding (gray), and construction frame (yellow)



Fig. 26 FNYM (inside the yellow frame) mounted on the vacuum vessel wall of the PF-1000

The significant advantages of the methods presented are: 1) Direct measurement of the fast neutrons emitted from the plasma column by applying the threshold reaction, which is sensitive to neutrons of energies above 919 keV; 2) the FNYM makes no record of the scattered neutrons of energies below the threshold; 3) the FNYM is useful in quickly re-measuring through the selection of a nuclear reaction giving a product with a relatively short half-life; and 4) In

contrast to the silver activation counters, the FNYM does not saturate and therefore there is no upper limit to its sensitivity.

5.1.2 Anisotropy of neutron emissions in the PF-1000 facility

In analyzing the multi-parametric function of the photon registration efficiency, I defined the geometry of the massive activation sample made of indium. The use of an optimized sample is important as the flux of emitted neutrons was limited by either the strength of the neutron source or the specific position of activation. Such situations occur for the PF-1000 plasma generator. Before the introduction of the massive, optimized indium sample, activation took place inside the vacuum chamber and initiated by a series of pulses. After the vacuum chamber was opened and samples were removed for measurement. The change in neutron emission for the subsequent discharge and the negative impact of opening the chamber to emit neutrons in later discharges became a characteristic feature of plasma focus (PF) devices. During the exposure series, there was of course no possibility of recording a single discharge. The use of massive samples introduced a definite change.

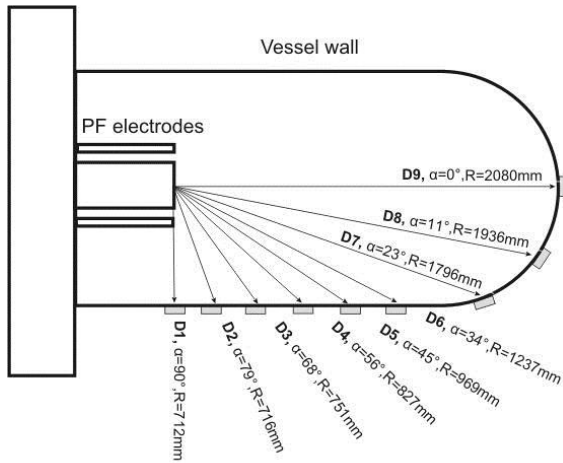


Fig. 27 Measurement of the neutron emission anisotropy by means of a nine massive optimized indium samples placed on the outside wall of the PF-1000 [M1]

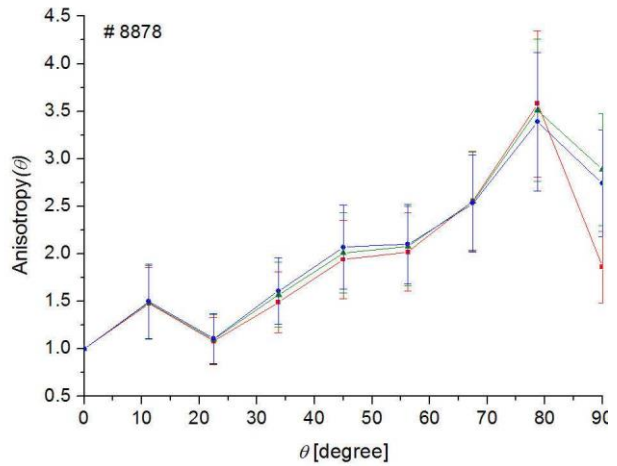


Fig. 28 Result of neutron emission anisotropy assessment for plasma discharge number #8876 from the activation of nine massive samples made from indium and supported by the MCNP calculation. The hypothetical locations of the neutron emission centers are as follows: ■ - 0 cm, ● -5 cm, ▲ -10 cm from anode surface [M1, J36]

The multi-parametric function of the photon registration efficiency has been used to discover the geometry of the massive indium sample and determine the anisotropy of neutron emissions from the PF-1000 facility [M1]. I placed nine massive indium samples outside the vacuum chamber of the PF-1000 device and exposed them to neutrons emitted from a single discharge. The samples were arranged on a plane passing through the main axis of the device. A diagram of the measurement arrangement is shown in Fig. 27. After activation, samples were measured using a γ -spectrometer. It surveyed the activity of two isotopes of indium: ^{115m}In and ^{116}In . To determine the anisotropy modeling, MCNP was used. The anisotropy of neutron emissions for the PF devices provides relevant information about generating neutrons. The neutrons in this system are produced as a result of two phenomena: thermonuclear fusion of deuterons and, for the vast majority, beam-target interaction. The relatively high coefficient of anisotropy indicated a high impact of the beam-target process, which occurred even outside the plasma column. The discharge anisotropy, measured as the ratio of the number of neutrons

emitted at an angle of 0° to those at 90° , reached 3.5. Fig. 28 shows the anisotropy for the other directions in neutron emission and their three hypothetical centers. They were assumed on the axis of the system at a distance of 0 cm, 5 cm, and 10 cm from the anode. I concluded that the fluctuations in the neutron source along the axis of the device did not affect the anisotropy. In paper [M2], results were also reported of the study on anisotropy in neutron emissions in a PF-1000 device using this method.

The significant advantages of the method presented are: 1) Effective application in the studies of plasma generated in PF-1000, massive indium samples for which the geometry developed using the theory of multi-parametric function of the photon registration efficiency; 2) The capability to assess the characteristics of a single plasma discharge; 3) Simultaneous testing of the emission of neutrons in nine different directions; and 4) To be able to infer that such a high rate of neutron emission anisotropy for a single plasma discharge ... "confirms the hypothesis that neutrons are produced mostly by intensive beams of fast deuterons, which induce nuclear reactions in the pinched plasma as well as in the gas target filling the discharge chamber".... [M1].

5.1.3 Radial asymmetry in the neutron emission for the PF-1000 device

I completed measurements of the neutron emissions across the axis of the PF-1000 device using massive indium samples. Eight massive indium samples were distributed on its outer wall, in a plane perpendicular to the axis of the device passing through the center of the plasma column (Fig. 29). The samples set were activated during a single discharge and the radioactivity of the indium isotopes were measured using γ -spectrometry. Based on the measured activity and MCNP calculations, I determined the neutron emission values at eight angles perpendicular to the axis of the system.

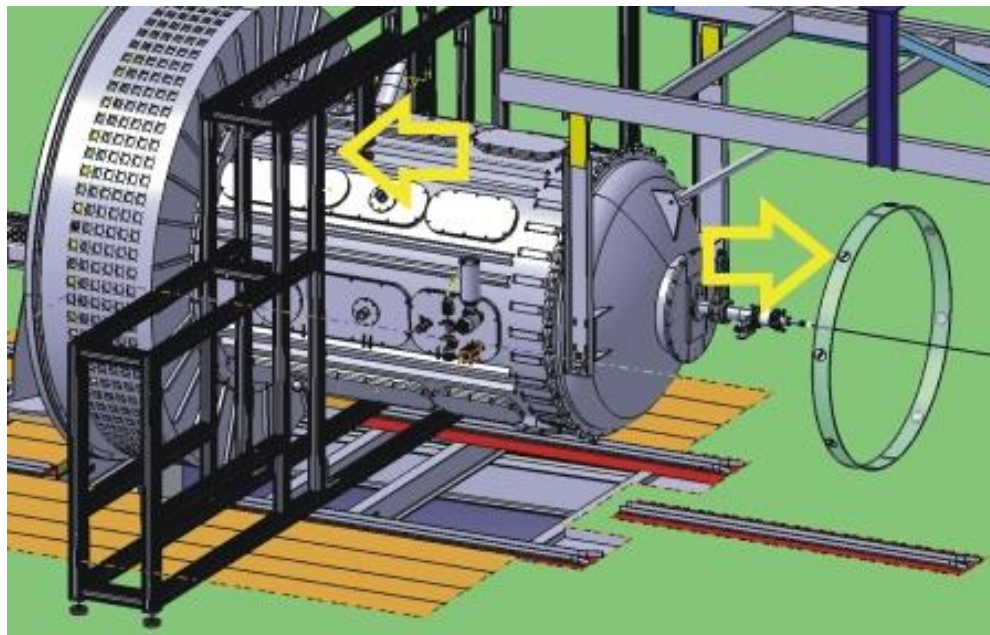


Fig. 29 Measurement of the radial neutrons emission for the PF-1000 device. The ring on the right is a virtual cut-out from the space indicated by the left arrow. On its surface, eight massive activation samples made from indium are visible

The following terms needed to be defined: Radial Distribution of Neutrons (RDN) denoted by R_{as} relates to the radial asymmetry of the neutron source, Shift of Neutron Emission Center

(SNEC) across the device axis, which is defined in terms of 1) α_s the neutron source rotation around the axis, and 2) R_s related to the relative displacement of the neutron sources across the device axis. R_{as} is expressed as:

$$R_{as} = \sum_{i=1}^8 \frac{|n_{AV} - n_i|}{n_{AV}}, \quad (11)$$

where n_{AV} is the average number of neutrons emitted during the relevant plasma discharge into the perigon lying in the plane perpendicular to the axis of the device and passing through the plasma column and n_i the number of neutrons emitted in the direction i . The value of R_{as} is in the range $(0, \infty)$; when near zero, the neutron source is deformed to a small extent, and its shape is close to circular (Fig. 30). In this plasma discharge, R_{as} reaches its lowest value of the observation. With the growth of R_{as} , the deformation of the neutron source also increases. An example of the above is presented in a plasma discharge registered as Shot No. #8920 (Fig. 31), for which the greatest deformation is seen. For the observed plasma discharges, the deformation did not exceed a value of two. I found that the greater the number of neutron emissions, the lower is the R_{as} value (Fig. 32). However, there were departures from this principle. A measure of R_{as} is also R_s ; the offset of the neutron sources from the axis of device. I have shown that with the increase in the deformation of the neutron source, the center of the source is moving away from the axis of the electrodes (Fig. 33).

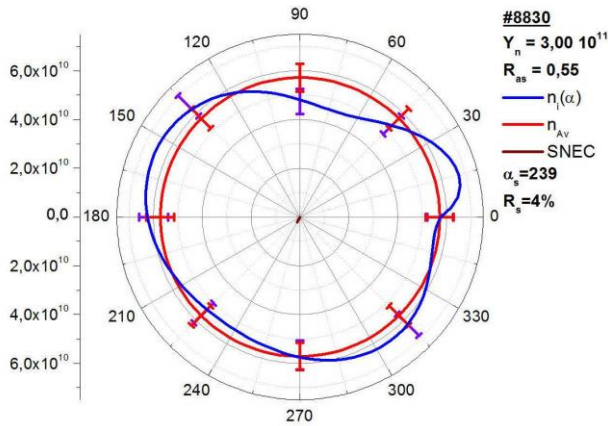


Fig. 30 RDN during a plasma discharge Shot No. # 8830 features the lowest observed deformation. Blue curve represents the deformed area of the neutrons emission; red curve represents the hypothetical undeformed source [M4]. Other definitions in Fig. 31

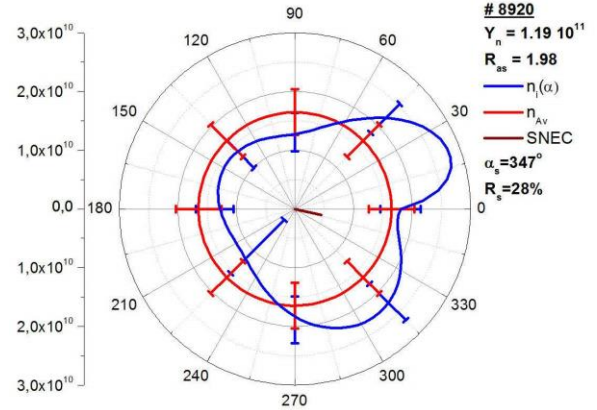


Fig. 31 RDN during plasma a discharge Shot No. # 8920 features the highest observed deformation. Brown line represents the displacement and rotation of the deformed center of the neutron emission across the axis of the device [M4, J36]

The methods presented offer significant advantages: 1) The effective use of the massive indium samples the geometry of which I developed theoretically using the multi-parametric function for the photon registration efficiency to study the RDN-radial distribution of neutrons for the PF-1000 device, 2) The enhancement in describing the emissions of neutrons of new terms such as R_{as} —the radial asymmetry of the neutron source, SNEC—the displacement of the neutron source across the device axis, α_s —the rotation of the neutron source around the device axis, and R_s —the relative displacement of the neutron source across the device; and 3) The demonstration that a neutron source in a PF-1000 device need not be positioned on the axis

of the system, and the shape of the source need not be symmetrical, which resulted in the monitoring of neutron emissions at a single point, e.g., using silver activation counters, can lead to erroneous results in the evaluation of Y_n [M4].

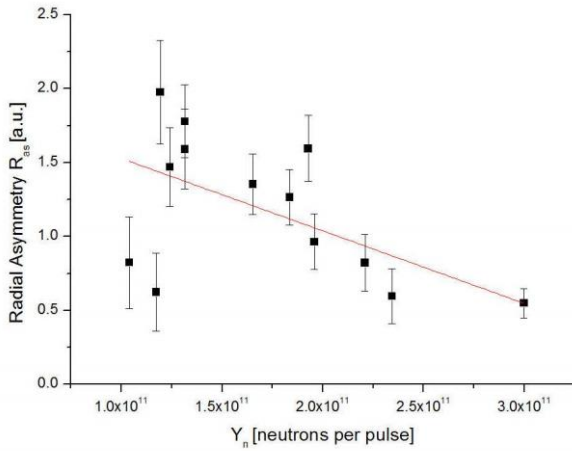


Fig. 32 Radial asymmetry of the emission of neutrons in the PF-1000 device decreases with increasing neutron emission efficiency. There are departures from this rule [M4, J36]

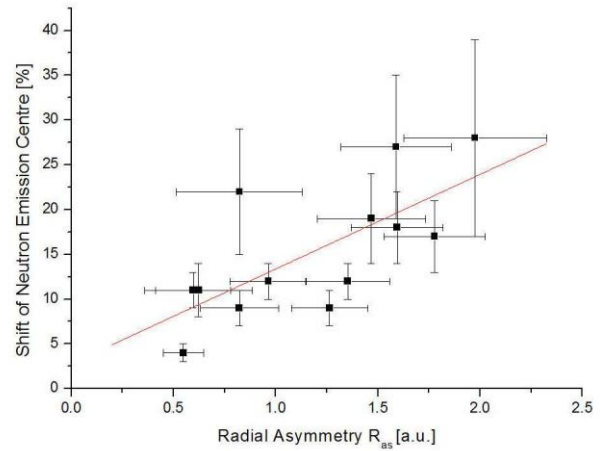


Fig. 33 With greater radial asymmetry, the greater the shift in the emission source of neutrons across the axis of the electrodes [M4]

5.2 Monitoring neutron yield Y_n for the 14-MeV neutron generator

Using the methodology presented in Section 4.2, I performed preliminary work [M6], aimed at testing the methods for assessing Y_n measured for the neutron generator (NG). The objective was the implementation of a method developed at Institute of Plasma Physics and Laser Microfusion for determining emissivity of the NG at 14-MeV. The study included monitoring the NG-type SODERN Genie 16 operated by the National Center for Nuclear Research. Another NG was used for the calibration of apparatuses for measuring neutrons at the JET tokamak.

I used the method described in detail above in the optimization of another activation sample geometry. The study was performed this time for yttrium. The optimal dimension for this purpose was a sample with a diameter of 80 mm and a height of 5 mm. I calculated the efficiency of photon registration using the methods presented above. The IAFEPE for a sample with the described above geometry is much higher than for the 18-mm diameter yttrium samples applied at the JET tokamak. The AFEPE determined for photons with an energy of 909 keV emitted from a metastable product of the nuclear reaction $^{89}\text{Y}(n, n')^{89m}\text{Y}$ was $(2.15 \pm 5)\%$. The reaction rate was estimated to be $6.45 \cdot 10^{21} (\pm 5.77\%) \text{ reaction} \cdot \text{s}^{-1}$, respectively. The emission rate for the above NG defined as the total number of neutrons emitted per unit time was $1.04 \cdot 10^8 (\pm 10.88\%) \text{ n} \cdot \text{s}^{-1}$. This value was in good agreement with data obtained from other sources (e.g., the manufacturer's specifications).

The methods presented provide significant advantages: 1) Yttrium is well activated by the 14-MeV neutrons—it has a relatively high cross section; 2) The sample geometry, as determined by the analysis using the multi-parametric function of the efficiency, resulted in a high photon registration efficiency with regard to the applied measurement geometry; 3) The large mass of the sample, which is conducive to efficient activation, resulted in a good statistical significance for the spectroscopic measurements; 4) The short half-life of the resulting radionuclide implies a rapid disintegration of the metastable nuclei yttrium, and hence a short

delay time for the next sample activation; and 5) NG(s) change their performance over time, and therefore their users are equipped with a reliable method of monitoring Y_n .

5.3 Investigating neutron emissions from deuterium plasma produced in the JET tokamak

The paper [M7] describes the application of the activation technique for the investigation of the neutron emissions from the deuterium plasma generated at the JET tokamak. It was useful in determining the dependence of the photon registration efficiency on the sample density ρ and in particular Z_{eff} . Based on the relevant calculations and data presented in Fig17A in the investigation of the 2.5-MeV neutrons emitted from plasma originating from the reaction of (d,d), the following nuclear reactions were applied: $^{47}\text{Ti}(n,p)^{47}\text{Sc}$, $^{54}\text{Fe}(n,p)^{54}\text{Mn}$, $^{58}\text{Ni}(n,p)^{58}\text{Co}$, $^{77}\text{Se}(n,n')^{77m}\text{Se}$, $^{79}\text{Br}(n,n')^{79m}\text{Br}$, $^{87}\text{Sr}(n,n')^{87m}\text{Sr}$, $^{89}\text{Y}(n,n')^{89m}\text{Y}$, $^{90}\text{Zr}(n,n')^{90m}\text{Zr}$, $^{111}\text{Cd}(n,n')^{111m}\text{Cd}$, $^{115}\text{In}(n,n')^{115m}\text{In}$, $^{167}\text{Er}(n,n')^{167m}\text{Er}$, $^{177}\text{Hf}(n,n')^{177m}\text{Hf}$, $^{197}\text{Au}(n,n')^{197m}\text{Au}$, and $^{207}\text{Pb}(n,n')^{207m}\text{Pb}$. With samples of these metals measured with HPGe detector, I estimated the efficiency of the photon registration as a function of sample density.

During the synthesis of deuterium in the JET tokamak a process of triton burn-up (TB) takes place. As a result of TB, 14-MeV triton burn-up neutrons (TBN) are produced. They are the result of the (d,t) reaction. Analysis of this process is of particular importance for the functioning of the International Thermonuclear Experimental Reactor (ITER) based on the synthesis of deuterium and tritium (t,d). For the study on TBN at the JET tokamak, the following nuclear reactions were in use: $^{27}\text{Al}(n,p)^{27}\text{Mg}$, $^{27}\text{Al}(n,\alpha)^{24}\text{Na}$, $^{46}\text{Ti}(n,p)^{46}\text{Sc}$, $^{48}\text{Ti}(n,p)^{48}\text{Sc}$, $^{56}\text{Fe}(n,p)^{56}\text{Mn}$, $^{59}\text{Co}(n,\alpha)^{56}\text{Mn}$, $^{59}\text{Co}(n,2n)^{58}\text{Co}$, $^{64}\text{Zn}(n,2n)^{63}\text{Zn}$, $^{90}\text{Zr}(n,p)^{90}\text{Y}$, $^{90}\text{Zr}(n,2n)^{89}\text{Zr}$, $^{93}\text{Nb}(n,2n)^{92}\text{Nb}$, $^{92}\text{Mo}(n,2n)^{91}\text{Mo}$, $^{197}\text{Au}(n,2n)^{196}\text{Au}$, and $^{204}\text{Pb}(n,n')^{204m}\text{Pb}$. For the above-mentioned target materials, I estimated the dependence of the photon registration efficiency on the activated material density.

Based on the knowledge gained in the analysis of the dependence on ρ of the multi-parametric function for the photon registration efficiency, in studying the plasma generated in the JET tokamak, a whole spectra of samples of mixed composition was offered: Mix1 [Al(17%), Hf(18%), Cd(32%), Y(21%), Se(5%), AlBr₃ (7%)], Mix2 Y(16%), Se(31%), AlBr₃ (53%)], Mix3 [Y(24%),Se(43%),Cd(33%)], Mix4 [Se(52%), Y(48%)] Mix5 [Se(40%), Y(40%), Al(20%)], Mix6 [Y(49%), Se(16%), Fe(15%), Si(20%)], Mix7 Y(40%), Fe(20%), Si(20%), Cu(20%)], Mix8 Y(47%), Se(16%), Al(16%), Fe(20%), Au(1%)], Mix9 [Y(48%), Se(16%), Al(16%), Fe(20%)], Mix10 [Y(50%), Se(16%), Al(17%), Fe(17%)], Mix11 [Y(48%), Se(16%), Al(20%), Fe(16%)], Mix12 [Y(40%), Al(30%), Fe(30%)], Mix13 [Fe(40%), Al(55%), Cu(5%)], Mix14 [Y(57%), Cu(43%)], and Mix15 [Y(36%), Si(64%)]. For all sample geometries, an energy-efficiency calibration of the detector was performed.

The reaction rates determined by this method are in good agreement with the values obtained using MCNP code. Work aimed at reconstructing the TBN spectrum is in progress.

The methods presented yielded significant advantages: 1) The use of a wide number of activation materials—unparalleled in scale to date; 2) The precise determination of the registration efficiency for photons emitted from the metal samples based on mathematical method; 3) The application of mixed samples (Mix) with high registration efficiency for photons emitted from these samples, which has contributed significantly in improving the efficiency of research—a single spectrometric measurement has yielded information on many activation products and has shortened the measurement time while achieving low measurement errors; and 4) The obtained values of the reaction rates showed linearity with respect to Y_n and hence guaranteeing the accuracy of the method.

In paper [M9], I pointed out the prospects for the testing of thermonuclear fusion. In preparation for the Second Deuterium Tritium Experimental Campaign (EDT2) on the JET tokamak, the use of the multi-parametric function for efficiency was already taking place for the characterization of the neutron generator (NG). This took place at the National Physical Laboratory in Teddington, London, during 2015–2016. Based on the precisely characterized NG, "in vessel" calibrations were conducted of the apparatuses for neutron monitoring at the JET tokamak (fission chambers - KN1, activation monitors - KN2). The stability of the NG during the in-vessel calibration was monitored using the activation technique. This took place in January, 2017. The methods for activation enhanced with the multi-parametric analysis of the registration efficiency have been adopted to monitor the emission of neutrons during the experimental campaign: EDT2; T-T¹, D-D² to be held at the JET tokamak. It will be the last event ending the JET tokamak story.

5.4 Environmental radiation monitoring

The development of nuclear power and technology requires radiation monitoring of the environment. Using the multi-parametric function of efficiency, I performed an energy-efficiency calibration of the spectrometer designed for radiation monitoring. The spectrometer was equipped with a scintillation detector 1.5' LaBr₃(Ce) with a generic NCh. Commissioned with completing the above mission, I developed a mathematical model that enabled an energy-efficiency calibration to be performed based on the mathematical methods [M3].

Using 3D maps, I showed the changes in the registration efficiency of photons emitted from the flat contaminated areas with diameter ranges 0.1-1.0 m and 1-100 m [M3]. These maps are presented in Fig. 19 and Fig. 20 [M3].

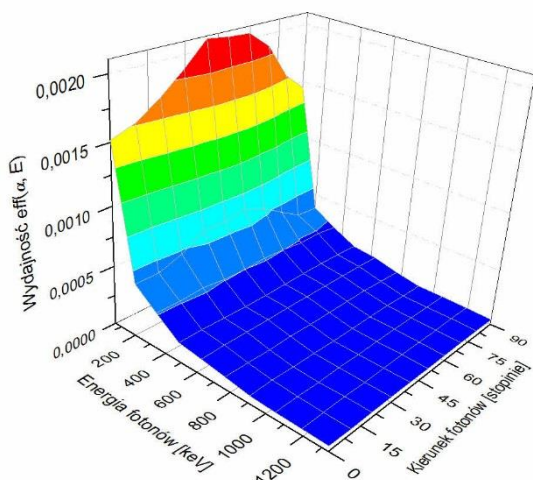


Fig. 34 Efficiency of the LaBr₃(Ce) detector as a function of the direction of photon incidence and photon energy determined with point calibration sources [M5]

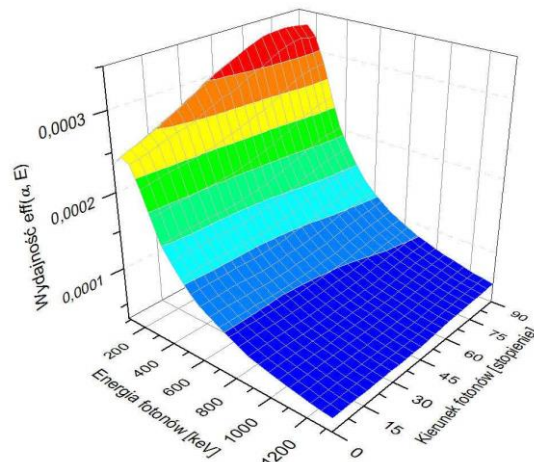


Fig. 35 Efficiency of the LaBr₃(Ce) detector as a function of the direction of photon incidence and photon energy determined using the multi-parametric efficiency function [M5]

Dealing with the point calibration sources, I experimentally confirmed the correctness of the mathematical model [M5]. Based on the multi-parametric function of the photon registration

¹ T-T is the name of the forthcoming experimental campaign at the JET tokamak, which will be filled with tritium.

² D-D is the name of the experimental campaign already held at the JET tokamak, which was filled with deuterium.

efficiency I plotted both the theoretical and the experimental efficiency as a function of the registered photon energy and the angle of photon incidence. This enabled the accuracy of the mathematical modeling to be determined (Fig. 34 and Fig. 35) [M5]. This demonstrates the importance of IAFEPE and SIAFEPE in evaluating the photon registration efficiency for radiation monitoring of the environment.

For the efficiency regarding the registration of radiation emitted from a contaminated infinite flat circular surface, I established a universal calibration curve expressed as

$$Eff(E)_{D \rightarrow \infty} = A_0 + A_1 \ln E + A_2 \ln E^2 + A_3 \ln E^3, \quad (12)$$

where

$$A_n = y_{n,0} + A_{n,1} \cdot \text{Exp}\left(\frac{-D}{t_{n,1}}\right) + A_{n,2} \cdot \text{Exp}\left(\frac{-D}{t_{n,2}}\right), \text{ for } n=0, 1,$$

$$A_2 = y_{2,0} + A_{2,1} \cdot \text{Exp}\left(\frac{-D}{t_{2,1}}\right), \text{ for } n=2,$$

$$A_3 = y_{3,0} + A_{3,1} \cdot \text{Exp}\left(\frac{D}{t_{3,1}}\right), y_{n,0},$$

with $A_{n,1}$; $A_{n,2}$; $t_{n,1}$; $t_{n,2}$ fitting parameters, and D the diameter of the contaminated area, S .

6 Accuracy

The accuracy of the mathematical energy-efficiency calibration of the HPGe detector with a dedicated NCh depends on the photon energy. This value varies from -7% SD for energy <150 keV, $\sim 6\%$ SD for energy range $150-400$ and $\sim 4\%$ SD for the energy range of $400-7000$ keV [M1, J37]. My own research, conducted on the HPGe detector and the Marinelli calibration source, showed that these values may exceed one tenth of a percent. For estimations related to the yttrium monitor and radiation monitoring, I processed only a generic NCh for the detectors NaI(Tl) and LaBr₃(Ce). The results obtained were less precise than those obtained using the dedicated characteristics of the HPGe detector. Based on a study using the NaI(Tl) detector and a cylindrical calibration, I demonstrated that the accuracy of the energy-efficiency calibration was in the range of $10-25\%$ depending on the photon energy. Hence, the estimation of Y_n for PF-1000 device is in the range of $15-30\%$. More accurate estimates for Y_n related to the discharge with greater neutron emissions because of the greater activity of yttrium induced in the sample therefore lead to better measurement statistics. Studies conducted using the point calibration source and the detector LaBr₃(Ce) showed that the angular registration efficiency for radiation monitoring was performed with an accuracy of $35-65\%$. Concerning radiation safety and protection, these values are acceptable.

7 Conclusions

The multi-parametric function for the photon registration efficiency was widely used in both neutronics and radiation monitoring.

In papers [M10-M12, J36, J37], I presented a complete description of the analytical methods for determining the multi-parametric efficiency function for photon registration.

I defined for the first time, new analytical methods to investigate various related functions of photon registration efficiency: IAFEPE, MIAFEPE, and SIAFEPE, and I have used them in

several applications. These methods enable different measurement geometries to be considered and the photon registration efficiency to be compared.

The registration efficiency was presented in the form of a 3D map as a function of many parameters.

This became the theoretical basis for designing the massive sample geometry. I applied these methods in studies described in several papers [M1, M2, M4, M6, M8].

Based on theoretical divagation and the experience gained previously [M2, M6, M8], I have proposed a new concept for measuring Y_n of many samples, the largest to date at the PF-1000 plasma generator. For this purpose, I constructed a fast neutron yttrium monitor [M 8].

Using a massive indium sample, I investigated the anisotropy of the neutrons emitted from the deuterium plasma generated by the PF-1000 device. This has contributed to a better understand of the mechanism of neutron generation in PF phenomena, in particular, in the PF-1000 device.

I completed an innovative study of the RND and introduced new concepts for describing the radial emission of neutrons for the PF-1000 plasma generator [M4].

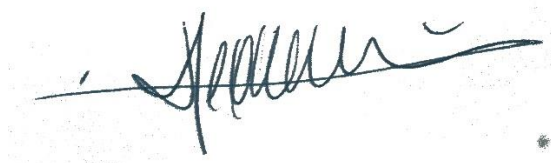
I created a theoretical basis and examined the dependence of the registration efficiency $eff(\rho, E)$ on sample density ρ and photon energy E . This enabled the application at the JET tokamak of dozens of different metals and radionuclides caused during neutron activation.

I have proved that increasing the sample density shifts the maximum efficiency, AFEPE, to a higher photon energy region. The maximum value of AFEPE diminishes with increasing photon energy. The IAFEPE behaves in a similar way (Fig. 17A–F). These studies resulted in establishing mixed samples for use in monitoring [M7]. Both types of samples have been effectively implemented at the JET tokamak.

The method employing the multi-parametric efficiency function is used to prepare and conduct DTE2 at the JET tokamak in 2019. They have been using previously described measurement geometries: a cylinder to measure the aluminum and iron activations and a "rosette" to measure niobium (Jednorog et al. Activation measurements in support of the 14-MeV neutron calibration of JET neutron monitors (in print). I have described the preparations for DTE2 in [M9, J36, J37].

I have shown the usefulness of the multi-parametric efficiency function for radiation monitoring, thereby extending the application possibilities of γ -spectrometry [M3, M5]. I have determined the universal efficiency function for *in situ* spectrometer equipped with a 1.5'-scintillator LaBr₃(Ce). For the same spectrometer, I have determined the dependence of the efficiency on incident photon direction.

The NCh for a γ -radiation detector makes it possible to perform mathematically efficiency calibrations for an unlimited number of different radiation sources. The results of the efficiency calibration of the detector with a dedicated NCh of high accuracy are comparable to those for energy-efficiency calibrations performed with calibrated sources.

A handwritten signature in black ink, appearing to be 'J. Jednorog', written over a horizontal line.